High-performance three-body near-field thermophotovoltaic energy conversion

Chunzhuo Dang[1], Xianglei Liu[1, *], Haifeng Xia[2], Shizheng Wen[1], Qiao Xu[1],

[1] School of Energy and Power Engineering, Nanjing University of Aeronautics and Astronautics, Nanjing 210016, China

[2] Hengli Eletek Co.,Ltd

E-mail: xliu@nuaa.edu.cn

Abstract: Abstract: Three-body structures have shown great potentials in enhancing the heat transfer rate and controlling the radiation spectrum in the near-field region, whereas are rarely considered in improving near-field radiative energy conversion performance. Here, a three-body thermophotovoltaic system configured by a tungsten emitter, a metallic spectral control layer, and a $In_{0.18}Sb_{0.82}Ga$ photovoltaic cell is considered. By parameter optimization of the spectrum control layer, the efficiency and output power at the gap distance of 10 nm are enhanced from 24.7% and 1.88×10^5 W/m^2 to 43.9% and 6.08×10^5 W/m^2, respectively. The potential mechanism lies in the excitation of coupled surface plasmon polaritons of the metallic spectral control layer. This work paves the way for applications of three-body structure in thermophotovoltaic systems and designing high-performance energy conversion systems.

Keywords: Near-field, thermophotovoltaic, three-body, spectrum control, surface plasmon

1. Introduction:

Ever-increasing energy demands require proper solutions to harvest enormous rejected thermal energy in industry[1, 2]. Thermoelectric generators are the most widely used solid-state heat-to-electricity techniques for this purpose but suffer from low efficiency[3]. As an alternative approach, the thermophotovoltaic (TPV) system has a higher efficiency and is more favorable[1, 4]. A TPV system is usually composed of a high-temperature emitter and a photovoltaic cell receiver with a low temperature. The photovoltaic cell receives thermal radiation from the emitter and converts it into electrical energy[5]. Since the TPV system can utilize different heat sources, it's versatile in applications such as solar energy collection and waste heat recovery[6, 7]. Possessing desirable features including simple components, no moving parts, and compact structures, TPV systems have got intense attention in recent years[5, 6, 8-15]. Despite all that, one bottleneck challenge of TPV system is its low output power, restricted by the blackbody radiation limitation[14].

Fortunately, people have found that when the gap distance between the thermal emitter and the photovoltaic cell is reduced below the value of characteristic wavelengths, the radiative heat flux can break the limit of blackbody radiation and the power density can far exceed that in the far-field system[16-20]. In near-field TPV systems, tunable evanescent waves are leveraged to enhance output power. Since Whale and Cravalho firstly proposed the application of near-field thermal radiation in TPV devices in 1997[21, 22], many theoretical studies[2, 5, 17, 23-32] and experimental efforts [33-35] have been conducted By employing thin films, graphene layers, hyperbolic materials, gratings, etc.[2, 5, 25, 29-32, 36, 37], , people have

successfully improved the performance of the near-field TPV system. For example, Bright et al. proposed a receiver composed of a thin film cell and a backside gold mirror, this structure's efficiency enhancement reached the level of 35% compared to a semi-infinite cell[2]. Watjen et al. applied an optimized tungsten grating to replace a flat tungsten emitter, and an increase of 6% in efficiency has been theoretically demonstrated[5]. Nevertheless, compared with TPV systems' Carnot efficiency limit[6, 14], the efficiency still has much room for improvement and needs more researches.

Recently, three-body structures have been employed to control near-field thermal radiative heat transfer[38-47]. Zheng and Xuan first studied the effect of inserting an intermediate body on near-field radiative heat transfer properties between two objects[42]. They showed that that inserting doped silicon films can enhance the radiative heat flux while aluminum films have a suppression effect. Messina et al. placed a passive relay amplifier between two SiC plates and observed better monochromaticity of thermal radiation spectrum [38]. Inspired by these phenomena, we are wondering whether the three-body structure can be applied to enhance the performance of near-field TPV sytesm by tuning the radiation spectrum. o

In this article, we propose a three-body near-field TPV system and study its thermal radiative energy transfer and conversion performances. Dyadic green functions combined with fluctuation-dissipation theory are used to evaluate the energy transfer of three-body structures[7, 48]. First, considering that the 1D photonic crystal filter has been applied to tune the thermal radiation spectrum in the far-field[9, 10], we will

study its performance as the spectrum control layer in the near-field three-body system. Then, a thin metallic layer, whose dielectric functions are described by the simple Drude model, is considered. Effects of dielectric function parameters and vacuum gap distances on the system performance are investigated in detail, and corresponding underlying mechanisms are revealed.

2. Methods:

Fig. 1.(a) shows the configuration of the proposed TPV system. The emitter is tungsten; the receiver is a $In_{0.18}Sb_{0.82}Ga$ photovoltaic cell, and between themis the immediate spectrum control layer, separated from both the emitter and receiver with a vaccum gap of width d. Both the emitter and receiver are assumed to be semiifinite and their temperatures are set as $T_1 = 1500$ K $T_2 = 300$ K, respectively. Dielectric function parameters of tungsten and $In_{0.18}Sb_{0.82}Ga$ are obtained fromreferences [49, 50]. The whole system is assumed to extend infinitely in the plane perpendicular to the z-axis.

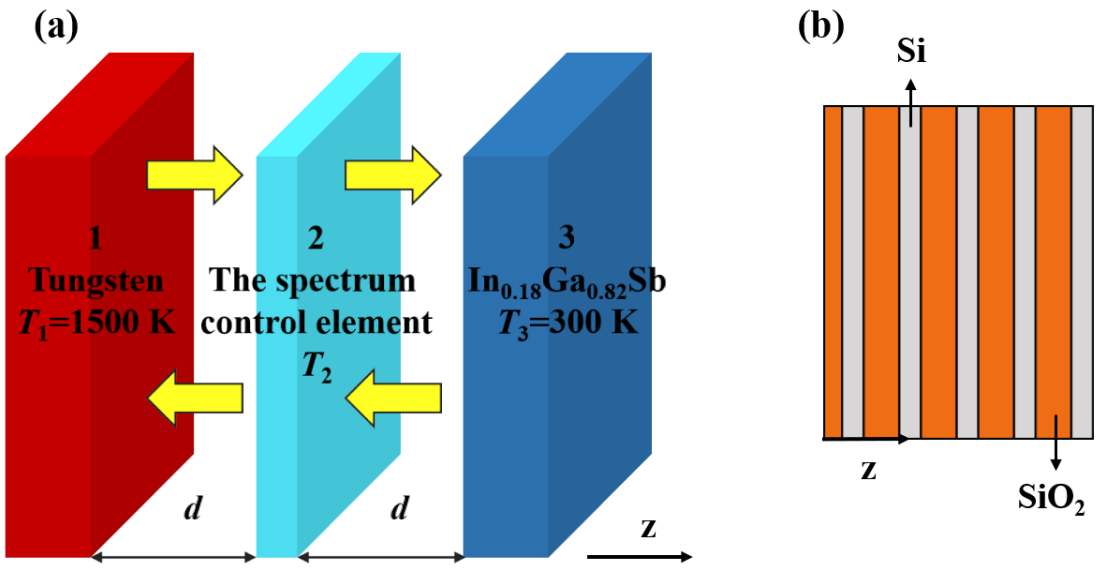

Fig. 1. (a). Schematic of a three-body TPV system. The parameters of the emitter and

receiver are fixed. The structure of the spectrum control element is replaceable, and its temperature needs to be solved based on energy balance. (b). Schematic of the modified quarter-wave stack filter composed of Si/SiO_2 $(L/2H(LH)^4)$.

As an indirect bandgap material, the dark current characteristics of the $In_{0.18}Sb_{0.82}Ga$ cell are controlled by minority carriers. The dark current is equal to the saturation current [51, 52]. Ignoring surface and bulk recombination, each photon reaching the photovoltaic cell with an energy higher than its energy gap E_g can generate a pair of electron-hole pairs. The electrical power P_{el} can be calculated by using methods mentioned in Refs.[17, 53]. The conversion efficiency can be calculated as $\eta = P_{\mathrm{el}}/P_{\mathrm{R}} \times 100\%$. The calculation method of the total radiative heat flux P_{R} will be listed later.

First of all, we choose typical photonic crystal filters as the spectrum control layerThe one-dimensional photonic crystal we employ is composed of alternating layers of Si and SiO_2. It is well known that there is a wavelength interval for non-propagating modes, for which the reflectivity is very high. We can calculate the bandgap central wavelength as [9]:

$$\lambda_0 = \frac{1}{2}\left(1+\frac{2+\frac{4}{\pi}\sin^{-1}\frac{n_2-n_1}{n_2+n_1}}{2-\frac{4}{\pi}\sin^{-1}\frac{n_2-n_1}{n_2+n_1}}\right)\lambda_g \tag{1}$$

where $n_1 = 1.5$ and $n_2 = 3.4$ is the refractive index of SiO_2 and Si, respectively [9]. The bandgap central wavelength is calculated to be λ_0=2.97 μm. Although n_1 and n_2 are fixed values when calculating the bandgap central wavelength, we still use the wavelength-dependent refractive index from Palik[49] when calculating the

radiative heat transfer. Next, we can calculate the thickness of layers: $L: t_1 = \lambda_0/(4n_1) = 0.495\ \mu\text{m}$, $H: t_2 = \lambda_0/(4n_2) = 0.218\ \mu\text{m}$. L refers to the material SiO_2 with a low refractive index, which corresponds to the thickness t_1; H refers to the material Si with a high refractive index, which corresponds to the thickness t_2. We chose the optimized $L/2H(LH)^4$ structure (shown in **Fig. 1.**(b)) instead of the initial $(LH)^5$ structure. By reducing the thickness of the first layer from left to half of the original, we can reduce the oscillation of the reflectivity in the passband and increase the energy transmission of the $\lambda < \lambda_g$ part[9]. Then, this structure is more suitable for a spectral control component.

Then we chose a layer of the Drude model as the spectrum control element. Its parameters will be optimized to make the near field TPV system have better performance. Generally, a Drude model will be given in the form $\varepsilon(\omega) = 1 - \omega_p^2/(\omega^2 + i\Gamma\omega)$ [54]. Here Γ is the loss term and ω_p is the plasma frequency.

The entire TPV system structure can be considered as a multilayer structure. The fluctuation-dissipation theorem and the dyadic Green's function are employed to calculate the heat transfer between any layers of this configuration. Essentially the Poynting vector is an energy flux, so the spectral heat flow from layer s to layer l is[5, 17, 48]:

$$q_{s\to l}(\omega) = \frac{1}{2}\left\langle \mathrm{Re}\left[\mathbf{E}(\mathbf{x},\omega)\times\mathbf{H}^*(\mathbf{x},\omega)\right]\right\rangle \tag{2}$$

where $\mathbf{E}(\mathbf{x},\omega)$ and $\mathbf{H}(\mathbf{x},\omega)$ is the electric and magnetic fields at $\mathbf{x}$, respectively. $\mathbf{E}(\mathbf{x},\omega)$ and $\mathbf{H}(\mathbf{x},\omega)$ are closely related to the source current at $\mathbf{x}'$ caused by the

thermal motion of charges or dipoles[55]:

$$\begin{cases} \mathbf{E}(\mathbf{x},\omega) = i\omega\mu_0 \int_V \bar{\bar{\mathbf{G}}}_e(\mathbf{x},\mathbf{x}',\omega)\cdot\mathbf{j}(\mathbf{x}',\omega)\,d\mathbf{x}' \\ \mathbf{H}(\mathbf{x},\omega) = \int_V \bar{\bar{\mathbf{G}}}_m(\mathbf{x},\mathbf{x}',\omega)\cdot\mathbf{j}(\mathbf{x}',\omega)\,d\mathbf{x}' \end{cases} \tag{3}$$

$\bar{\bar{\mathbf{G}}}_e(\mathbf{x},\mathbf{x}',\omega)$ and $\bar{\bar{\mathbf{G}}}_m(\mathbf{x},\mathbf{x}',\omega)$ are the corresponding electric and magnetic dyadic Green's function which convert the source current at $\mathbf{x}'$ to electric and magnetic fields at $\mathbf{x}$. Green's functions have been employed for thermal radiation in multilayer structures[56-59]. The spatial correlation between the fluctuating current densities at $\mathbf{x}'$ and $\mathbf{x}$ is necessary for calculating $q_{s\to l}(\omega)$, which is obtained by the fluctuation-dissipation theory. $q_{s\to l}(\omega)$ can be written as a form containing $\xi_{s,l}(\omega,\beta)$:

$$q_{s\to l}(\omega) = \frac{\Theta(\omega,T_s)}{\pi^2}\int_0^\infty \xi_{s,l}(\omega,\beta)\beta d\beta \tag{4}$$

$\Theta(\omega,T_s)$ is the average energy of the Planck oscillator . $\xi_{s,l}(\omega,\beta)=\xi_{l,s}(\omega,\beta)$ is the transmission coefficient between s and l. β is the transverse wave vector in the plane perpendicular to the z-axis. $q_{s\to l}(\lambda) = q_{s\to l}(\omega)\cdot\omega/\lambda$ is the form related to the wavelength of spectral heat flux $q_{s\to l}(\omega)$. The whole heat flux from the layer s to the layer l can be written as the integral of the spectral heat flux $q_{s\to l}(\lambda)$ over the wavelength: $Q_{s\to l} = \int_0^\infty q_{s\to l}(\omega)d\omega = \int_0^\infty q_{s\to l}(\lambda)d\lambda$. The net heat transfer between layers s and l is calculated as $q_{sl} = q_{s\to l} - q_{l\to s}$. The whole net heat flux Q_{sl} between layers s and l is calculated as $Q_{sl} = \int_0^\infty q_{sl}(\omega)d\omega = \int_0^\infty q_{sl}(\lambda)d\lambda$.

Now let's consider the heat transfer of the entire multilayer structure. In a stable working state, the system should be in a dynamic thermal equilibrium. The energy radiated by the spectrum control element to the rest of the system at any time should

be equal to the heat given to the spectrum control element by the rest of the system, which can be written as the relationship $\mathrm{Q}_{2\to1}+\mathrm{Q}_{2\to3}=\mathrm{Q}_{1\to2}+\mathrm{Q}_{3\to2}$. we can conclude that the real heat transfer between the emitter and receiver is:

$$P_{\mathrm{R}}=\mathrm{Q}_{1\to2}+\mathrm{Q}_{1\to3}-\mathrm{Q}_{2\to1}-\mathrm{Q}_{3\to1}=\mathrm{Q}_{1\to3}+\mathrm{Q}_{2\to3}-\mathrm{Q}_{3\to1}-\mathrm{Q}_{3\to2} \tag{5}$$

Because the spectrum control element has no support, its temperature will automatically change to a temperature that makes the system thermally balanced. We can assume a temperature TT for the immediate body and apply it to the equation $\mathrm{Q}_{2\to1}+\mathrm{Q}_{2\to3}=\mathrm{Q}_{1\to2}+\mathrm{Q}_{3\to2}$. Through iterative calculations, we can solve the correct $T2$, and then get the exact heat transfer capacity of the TPV system. It should be noted that when the spectrum control element has a multilayer structure (such as our 10-layer structure filter), $\mathrm{Q}_{2\to1}=\sum_{a=1}^{n}\mathrm{Q}_{2-a\to1}$, $\mathrm{Q}_{\mathrm{s}\to2}=\sum_{a=1}^{n}\mathrm{Q}_{\mathrm{s}\to2-a}$. Here a represents the sequence number of a layer in the spectrum control element, n is the total number of layers. ξ and $q(\lambda)$ also have the same processing method for the spectrum control element. We set the temperature of each layer to be the same.

Although the amount of heat radiated by the emitter and the amount of heat absorbed by the receiver at the same time is the same, the radiation spectrum at the two places is not the same due to the role of the middle layer. $q_{1\mathrm{out}}==q_{12}+q_{13}$ represents the spectrum of the radiation emitted from the emitter, and $q_{3\mathrm{in}}=q_{13}+q_{23}$ represents the spectral distribution of the radiation received from the receiver. $q_{3\mathrm{in}}$ is directly related to the energy conversion occurring within the photovoltaic cell.

3. Results and discussion

We have selected the integration range of λ from $0.22\ \mu m$ to $9.9\ \mu m$. Now we make the minimum interval in both systems consistent and they are d, and we set the x coordinate of the graph to d. We calculated the system's performance trend of the vacuum gap d from $10\ nm$ to $100\ \mu m$. For systems without the spectrum control element, we set the left vacuum gap to $0\ nm$ and the spectrum control element's width to $0\ nm$ in the program.

Now we will observe the performance of a one-dimensional photonic crystal filter in a three-body system. It can be seen from **Fig. 2**. (a) that when the gap is large than $10\ \mu m$, the efficiency of both TPV systems remain almost a constant, and the filter improves the conversion efficiency by about 2%. This is because in the far-field the transmission of energy mainly depends on the propagating wave and is not sensitive to changes in the gap's size[54]. In the far-field, the radiation heat transfer spectrum of the system does not change significantly with the variation of vacuum d. Under far-field conditions, one-dimensional photonic crystals are used to improve system efficiency by filtering. **Fig. 3**.(a) shows the spectral heat transfer diagram at $d = 100\ \mu m$ and proves that the filter does improve the efficiency of the system by reflecting the energy of $\lambda > \lambda_g$. For the reflectivity of the filter has a large vibration in the pass band, and the filter has unavoidable absorption within $\lambda < \lambda_g$, the spectral heat transfer of the TPV system with filter is lower[9]. Compared with the common TPV system, the three-body system's radiant heat exchange volume is reduced, resulting in a reduction in output power, as shown in **Fig. 2**.(b). As the gap becomes

smaller, the efficiency of both thermal photovoltaic systems began to decline after experiencing fluctuations. In this range, constructive interference and deconstructive interference in the vacuum gaps will change the energy transmission near λ_g [5]. In $\lambda > \lambda_g$, spectral heat transfer increases and the filter cannot completely filter. But at this time, the efficiency of the three-body system is still higher than that of common TPV systems. When the gap is further reduced, the efficiency of the three-body system is not improved and lower than the common TPV system's efficiency at $d = 1.5 \times 10^{-7}$ m. Since the vacuum gap is sufficiently small at this time, the evanescent wave is the dominant radiation heat transfer.

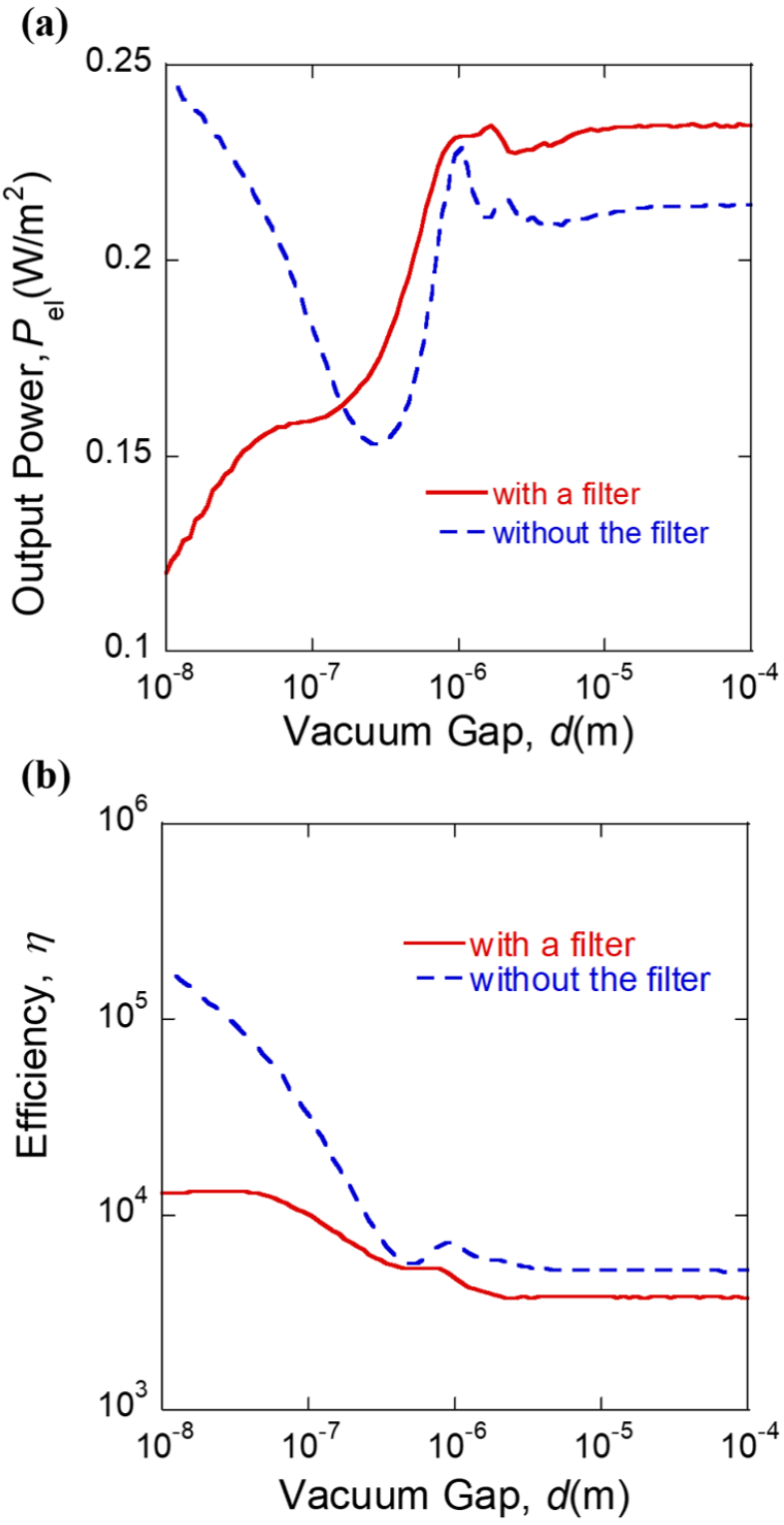

Fig. 2. (a) and (b) are the curves of the conversion efficiency and output power during the change of gap width d from 10 nm to 100 μm, respectively. The blue dotted line refers to the system without filter; the red curve refers to the three-body system.

Fig. 3.(b) shows that when the gap $d = 10\ \text{nm}$, the spectral heat transfer of the common TPV system is much higher than that of the three-body system. Moreover, the shapes of the heat transfer spectral curves of the two systems are also very different. In the region of $8\ \mu\text{m}<\lambda<10\ \mu\text{m}$, the spectral heat transfer of the three-body system has increased. At this time in the three-body system, the actual distance between the emitter and the receiver is $3.3375\ \mu\text{m}$. By comparison, We found that when the distance between the emitter and receiver was kept at $3.3375\ \mu\text{m}$, the filter improved the heat transfer capacity of the three-body system. In **Fig. 4**, we draw the contours of the related heat transfer coefficients for the three-body system when the vacuum gap is $d = 10\ \text{nm}$. **Fig. 4**.(a) shows the heat transfer coefficient between the common near-field thermal photovoltaic system's emitter and receiver. We can see that the improvement of the heat transfer situation of the common TPV system at $d = 10\ \text{nm}$ in **Fig. 4**.(a). **Fig. 4**.(b) is obtained by summing $\xi_{1,3}(\omega,\beta)$ corresponding to the heat exchange between emitter and receiver and $\xi_{2,3}(\omega,\beta)$ corresponding to the heat exchange between filter and receiver. $\xi_{1,3}(\omega,\beta)$ is roughly in the green rectangular frame and shows a strong interference phenomenon and there are evanescent waves. There are two areas of $\xi_{2,3}(\omega,\beta)$. In areas with high ω, it is almost dominated by the last layer $\text{Si}(\xi_{2-10,3}(\omega,\beta))$. In the low ω region, it is dominated by the penultimate layer $\text{SiO}_2(\xi_{2-9,3}(\omega,\beta))$. It can be seen that, because the thickness of the filter $t = 3.3175\ \mu\text{m}$ is far greater than the vacuum interval, the filter is considered to be semi-infinite, and the heat exchange between the filter and the receiver is almost completed by the last layer[38]. And

because $\xi_{2-10,3}(\omega,\beta)$ is distributed in the area of high ω, $\xi_{1,3}(\omega,\beta)$ migrates to high ω. Because of the existence of the filter, although the radiation emitted by the emitter and the radiation received by the receiver is the same amount, the radiation spectrum $q_{1\text{out}}$ and $q_{3\text{in}}$ are already different. Although $\xi_{2-10,3}(\omega,\beta)$ is very large and has a strong near-field effect, the heat transfer capacity of this part is small. This is because $\Theta(\omega,T_2)$ will become extremely small in the high ω region and the temperature $T_2=1148.8\ \text{K}$ of the filter will be much lower than the temperature $T_3=1500\ \text{K}$ of the emitter. The energy gap E_g of $\text{In}_{0.18}\text{Sb}_{0.82}\text{Ga}$ corresponds to $\omega_g=8.47\times10^4$. For the absorption spectrum of the entire three-body, the introduction of the filter leads to an increase in heat transfer in the region $\omega<\omega_g$, which will reduce the efficiency of the system. And there is a large heat exchange in the high ω area, and the excess energy will generate heat due to the heating in the cell, causing the efficiency to decrease.

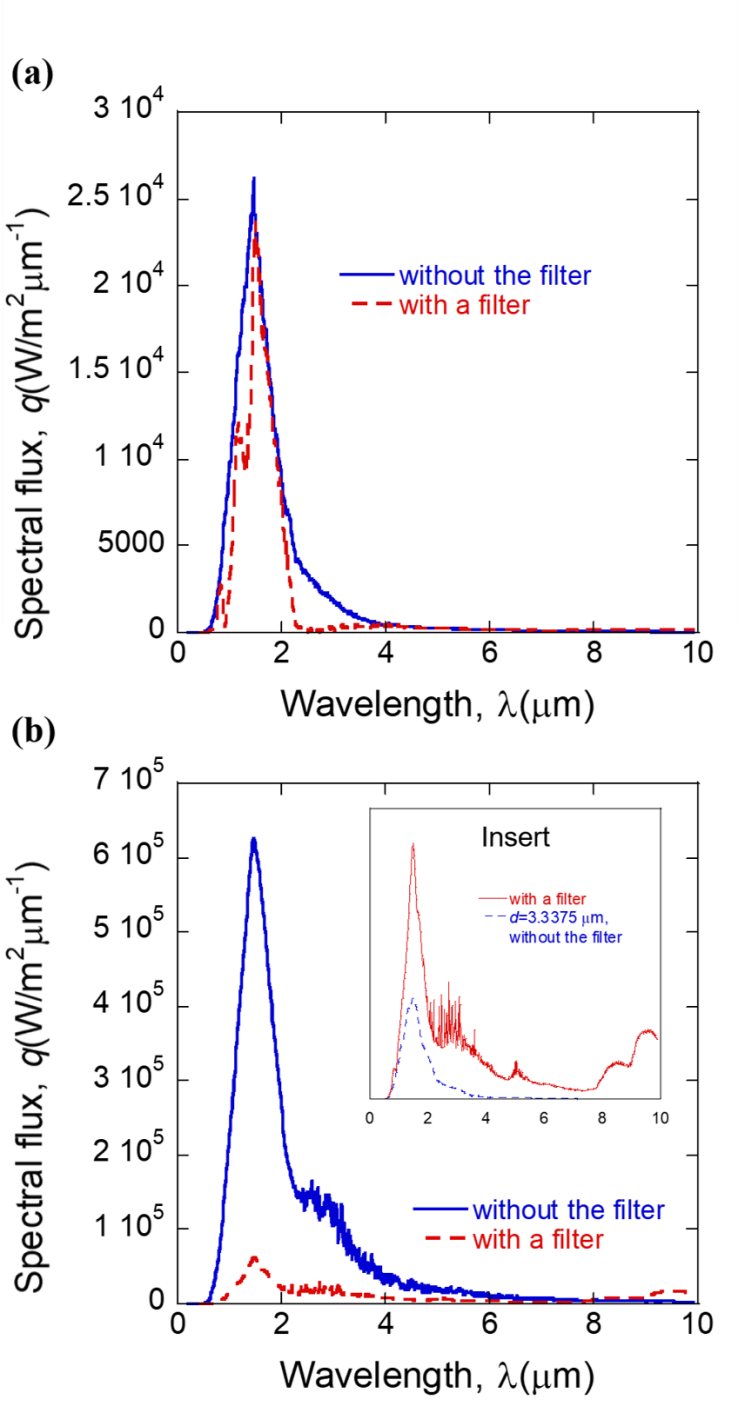

Fig. 3. Heat transfer spectrum of the TPV system. The blue curve is the heat transfer spectrum of the common TPV system without the filter. The red dotted line is the absorption spectrum $q_{3\text{in}}$ of the receiver in the three-body system (a). The gap d is 100 μm . (b) The gap d is 10 nm. The insert figure is a spectrum when the interval between the emitter and receiver is set to 3.3175 μm.

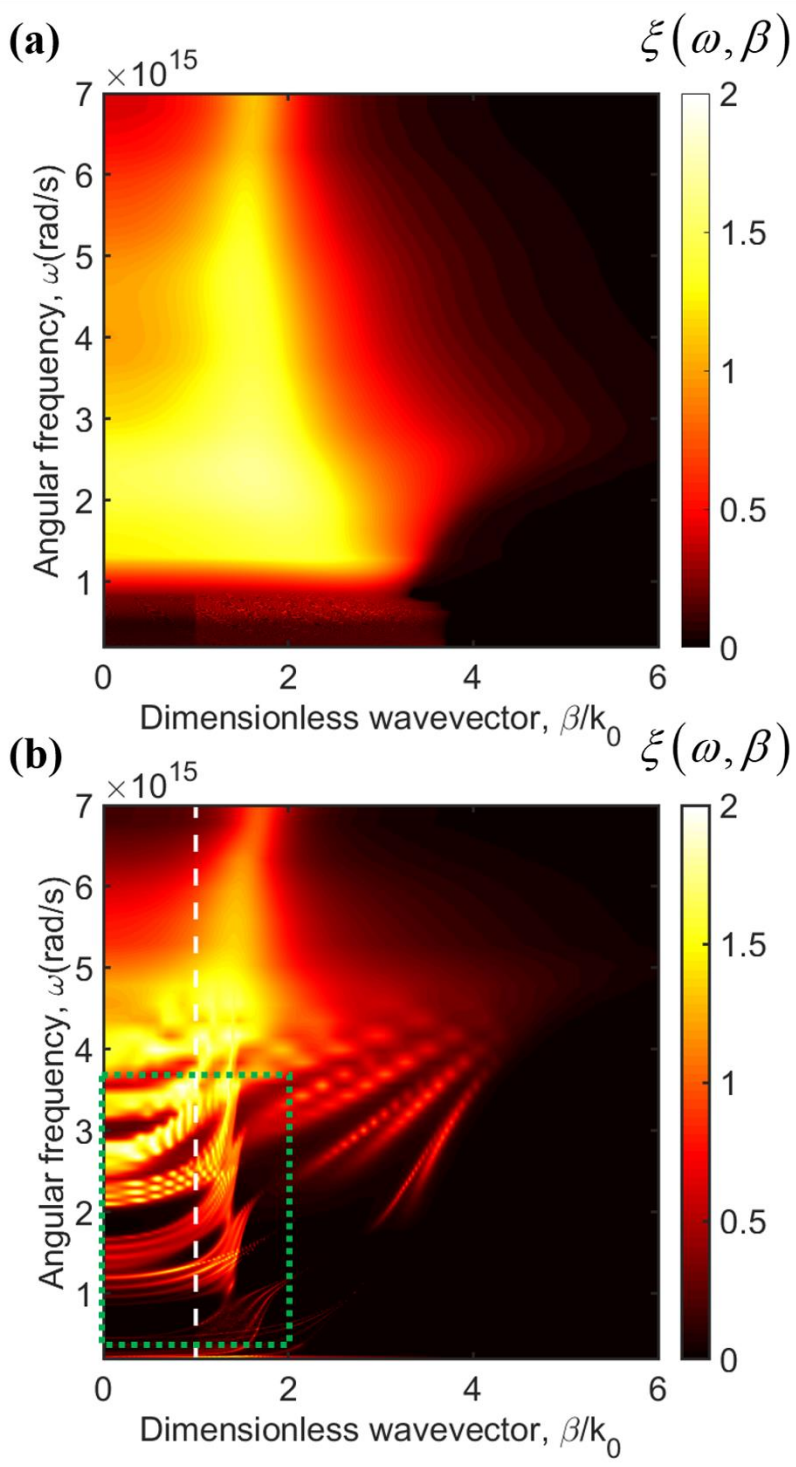

Fig. 4. Contours of heat transfer coefficients between components of the TPV system at $d = 10$ nm. (a). the heat transfer coefficient of the common TPV system without the filter. (b) $\xi_{1,3}(\omega,\beta)+\xi_{2,3}(\omega,\beta)$ of the three-body system. White dotted lines are light lines. $k_0 = \omega/c0$ is the wave vector in the vacuum.

So far, we have shown and explained in detail the effects of one-dimensional photonic crystals in near-field and far-field conditions. We have found that it does not improve the performance of near-field TPV systems. When the gap is small enough, the evanescent waves from both sides of the vacuum gap are coupled into each other. These evanescent waves have large transverse wave vectors, which cannot be filtered by one-dimensional photonic crystal filters[10]. And because the filter is too thick, the near-field performance of the filter's rightmost material and the $In_{0.18}Sb_{0.82}Ga$ photovoltaic cell will greatly affect the radiation heat transfer of the entire system. However, the far-field TPV system has its inherent limitation of low output power. To obtain high power, the near-field TPV system must be used. Therefore, we next study the characteristics that the spectrum control element should have based on near-field conditions.

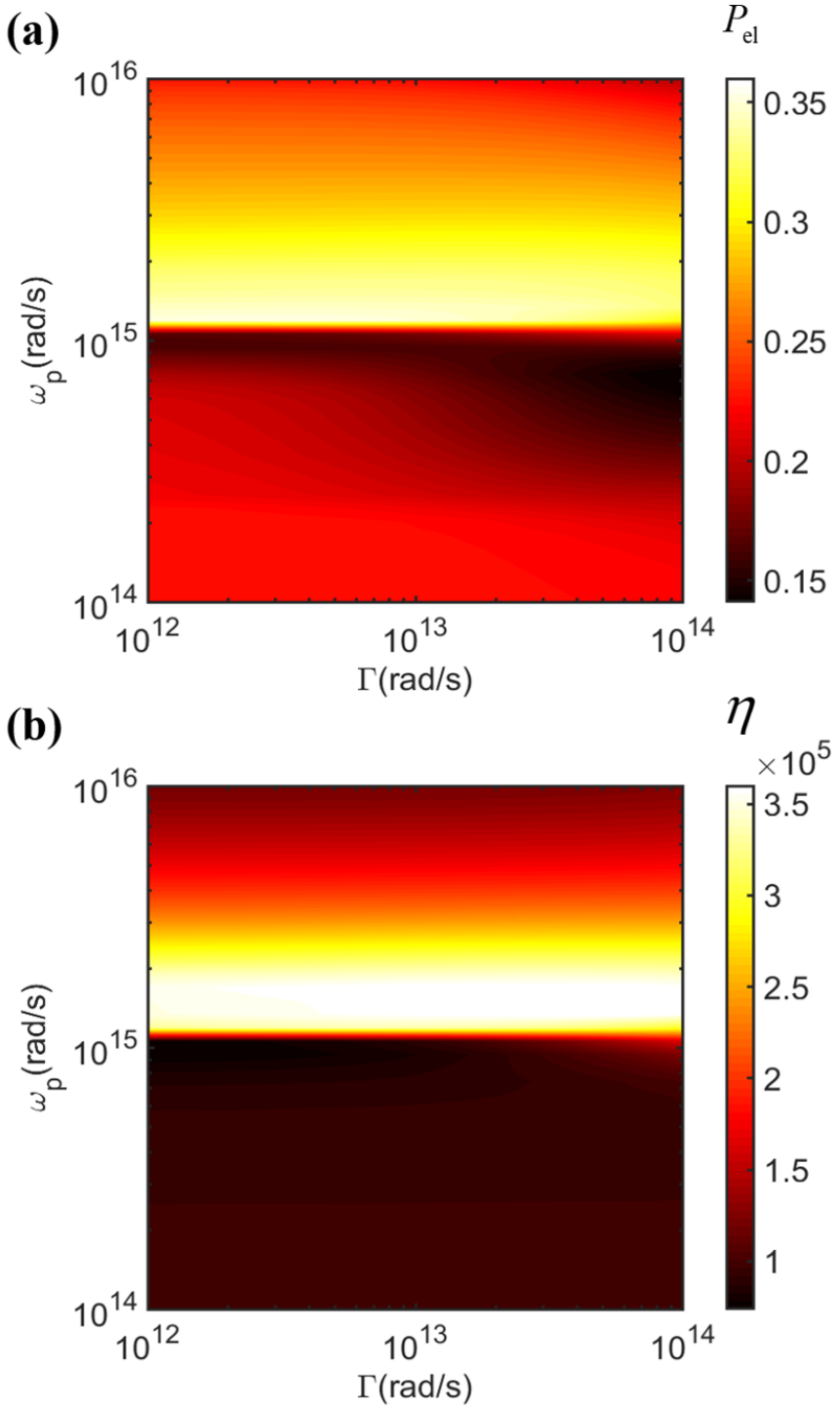

Fig. 5. Drude models with different parameters are combined by different values of ω_p and Γ. We placed a Drude model plate as the spectrum control element with width $t = 10$ nm in the near-field TPV system, and calculated the performance at the vacuum gap $d = 10$ nm :(a) conversion efficiency η. (b) output power P_{el}.

In this part, we study the role of Drude model plates formed from different combinations of ω_{p} from 1×10^{14} to 1×10^{16} rad/s and Γ from 1×10^{12} to 1×10^{14} rad/s in a three-body system. As shown in **Fig. 5**, in a large area, this near-field TPV system has shown good performance. Compared with the efficiency $\eta=24.7\%$ and the output power $P_{\mathrm{el}}=1.88\times10^{5}\ \mathrm{W/m^2}$ of the common near-field TPV system with a vacuum gap of $d=10\ \mathrm{nm}$, the optimized near-field three-body TPV system has a better performance. The maximum efficiency we obtain is 35.3%, the maximum power is $3.61\times10^{5}\ \mathrm{W/m^2}$, and when one of the two values is at its maximum, the other value will also get a relatively large value. This layer of the Drude model plate acts as a relay station so that energy transmission can be achieved at a large distance, and it also can control the spectrum. As can be seen from **Fig. 5**, $\omega_{\mathrm{p}}=1.2\times10^{15}$ rad/s is a clear dividing line for both parameters. For near field TPVsystems, we aim for higher conversion efficiency. We observe that in the range of $1.2\times10^{15}<\omega_{\mathrm{p}}<2.4\times10^{15}$ rad/s , $1\times10^{12}<\Gamma<1\times10^{14}$ rad/s , the system has a conversion efficiency of more than 30% and an output power higher than $3\times10^{15}\ \mathrm{W/m^2}$. Considering that the loss Γ should not be too small, we first select the Drude plate of $\omega_{\mathrm{p}}=1.2\times10^{15}$ rad/s, $\Gamma=2\times10^{13}$ rad/s for research. As shown in **Fig. 6**, the function of the immediate body at this time is not filtering. Because the system has good monochromaticity in the $\lambda<\lambda_g$ part and has a high peak, the number of photons that can be used to excite electron holes increases sharply, resulting in a significant increase in the conversion efficiency and output power of the system. If surface polarizing polarons are present in the system, a strong evanescent

wave can be excited[38, 60, 61]. For the Drude model film in the vacuum, its polarization dispersion relationship can be expressed as $\tanh(ik_{2z}t)(k_{2z}^2/\varepsilon_2^2+k_z^2)-2k_zk_{2z}/\varepsilon_2=0$ [54, 61], where $k_z=\sqrt{(\omega/c0)^2-\beta^2}$ is the component of the wave vector in the z-direction in the vacuum, $k_{2z}=\sqrt{\varepsilon_2(\omega/c0)^2-\beta^2}$ is the z-component in the Drude model film, ε_2 is the dielectric function. It contains the high-frequency asymmetric mode and the low-frequency symmetric mode. The high-frequency asymmetry mode $k_z+(k_{2z}/\varepsilon_2)\times\tanh(k_{2z}t/2i)=0$ is drawn in the green dotted line in **Fig. 7**.(a). Because the structure of the three-body system is more complicated, the high-frequency asymmetric mode is different from the SPP distribution of the system. But we can speculate that the improvement of system performance is due to the asymmetric mode of the coupled surface polariton. The intermediate plate provides a new heat transfer channel. **Fig. 7**.(a) shows that the heat transfer coefficient of the system is mainly distributed in two regions, namely the frustrated mode near $\omega=2\times10^{15}$ rad/s and the surface mode near $\omega=1.0\times10^{14}$ rad/s . The corresponding ω_{spp}, which is slightly higher than the bandgap width ω_g of the photovoltaic cell. **Fig. 7**.(b) shows that the immediate body stimulates the surface mode with the receiver to enhance the radiative heat transfer of the system, and improves the system's efficiency by improving the monochromaticity of the radiation spectrum. Since it is in a three-body system, this surface mode is also shown in $\xi_{1,3}(\omega,\beta)$[43]. The emitter has a higher temperature, which can further improve energy transfer. T_2 is more than 1400 K at this time. For the conventional TPV

system, due to the reason that the emitter's temperature is usually above 1000 K, many materials supporting strong evanescent mode cannot be applied as a result of their low melting points. Nonetheless, if we can actively control the temperature of the intermediate plate at a low level in the three-body system, such materials can be reconsidered. And we believe this approach of introducing new materials will further enhance the strength of evanescent mode in the TPV system, ultimately improving the performance of them. In **Fig. 5**, when $\omega_{\mathrm{p}} < 1.2\times10^{15}$ rad/s, the transmitted energy of the system is low and most of the photons cannot be used to stimulate the generation of electron-hole pairs, resulting in low efficiency. When $\omega_{\mathrm{p}} > 1.2\times10^{15}$ rad/s, due to the effect of SPP (surface plasma polarization), a strong radiant energy exchange can occur near ω_{spp}. The system's radiant heat transfer spectrum is concentrated in the area of $\omega > \omega_g$ ($\lambda < \lambda_g$), and the output power is significantly improved. However, when ω_{p} is further increased, the performance of the system is gradually reduced due to the thermalization in the cell. In the region of $\omega_{\mathrm{p}} > 1.2\times10^{15}$ rad/s, the performance of the system is not sensitive to changes in Γ. But the increase of loss Γ will make the system efficiency decrease slowly.

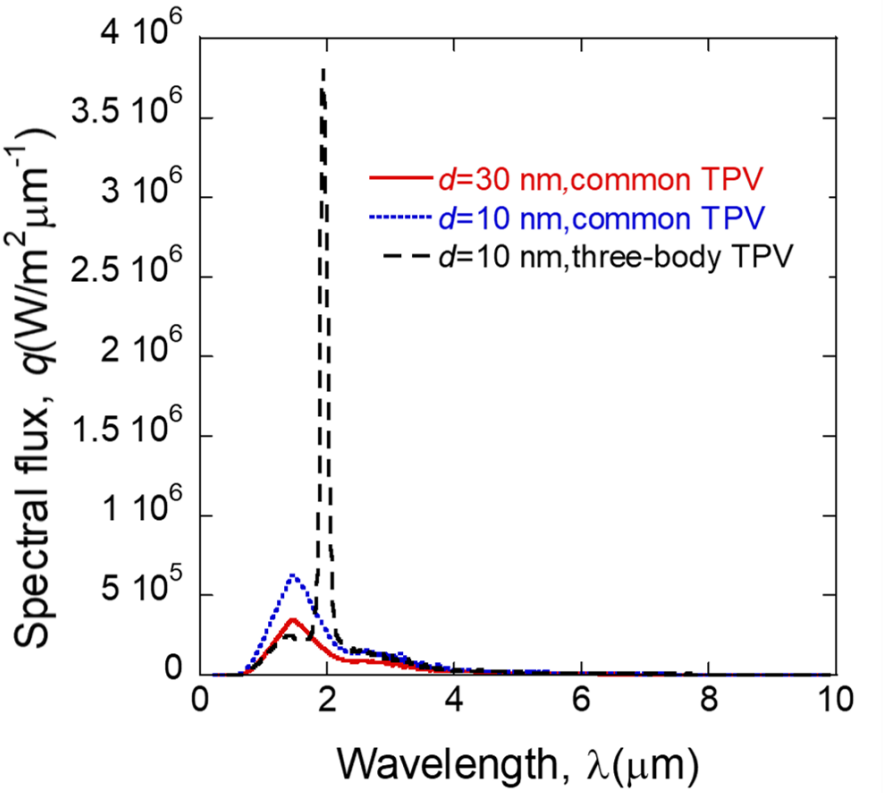

Fig. 6. The spectral distribution: the red curve is the spectral distribution of the common system heat transfer at $d = 30$ nm; the blue dotted line is the spectral distribution of the common system heat transfer at $d = 10$ nm; the black dotted line is the spectral distribution of the three-body system heat transfer at $d = 10$ nm, $t = 10$ nm, $\omega_p = 1.2\times10^{15}$ rad/s, $\Gamma = 2\times10^{13}$ rad/s.

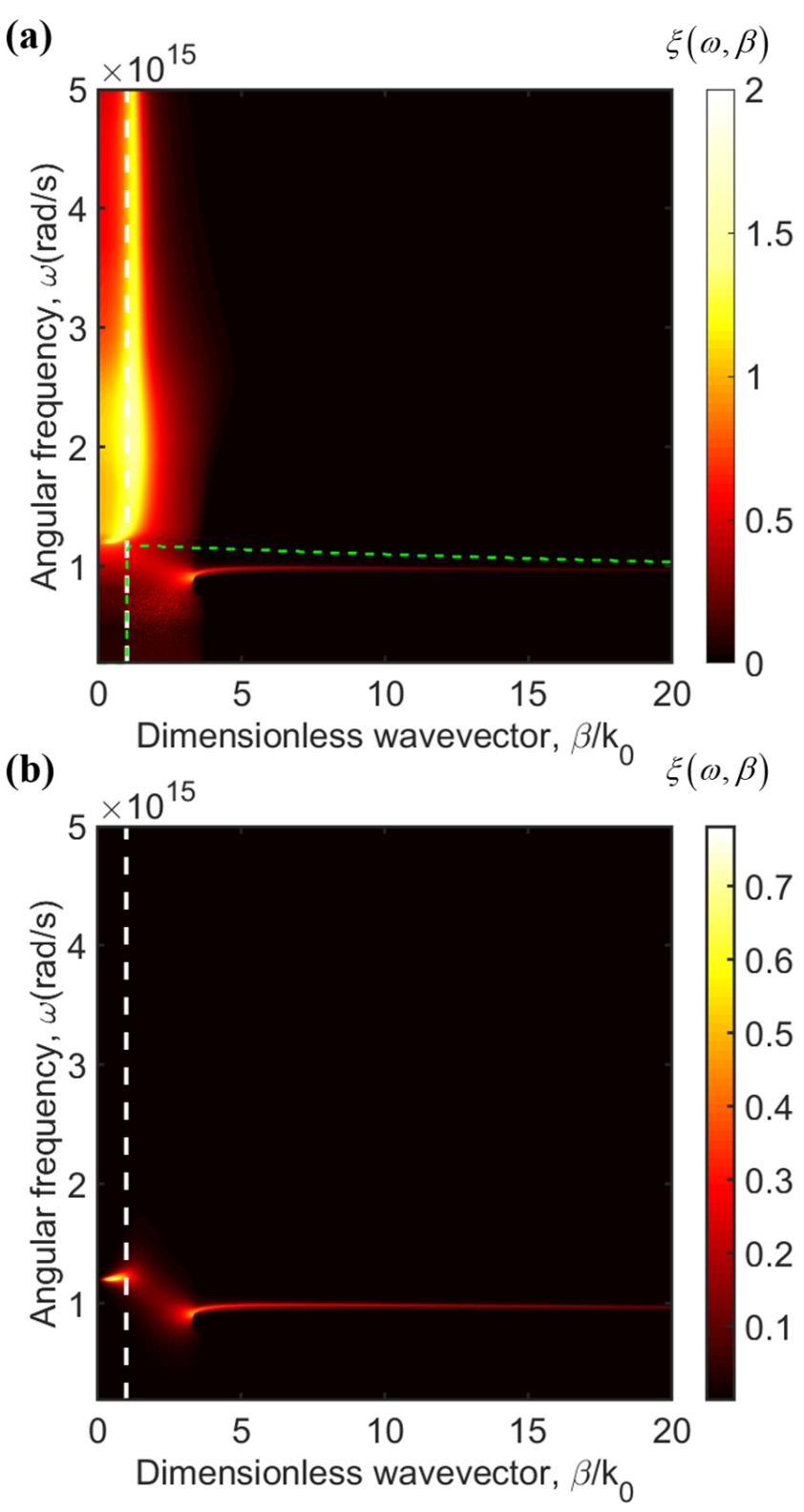

Fig. 7. (a) $\xi_{1,3}(\omega,\beta)+\xi_{2,3}(\omega,\beta)$ and (b) $\xi_{2,3}(\omega,\beta)$ of the three-body TPV system at $d=10$ nm, $t=10$ nm, $\omega_p=1.2\times10^{15}$ rad/s, $\Gamma=2\times10^{13}$ rad/s. White dotted lines are light lines. $k_0=\omega/c0$ is the wave vector in the vacuum.

In **Fig. 8**, we plot the variation of the performance of the optimized Drude model plate at $\omega_{\mathrm{p}}=1.2\times10^{15}\,\mathrm{rad/s},\Gamma=2\times10^{13}\,\mathrm{rad/s}$ with the vacuum gap. It can be seen that the performance of the three-body system with the plate based on the near field design changing with the vacuum gap d is similar to that of the ordinary thermal photovoltaic system. Because the system improves its efficiency by relying on a near-field mechanism, the performance of the system rapidly decays as the gap increases. In the far-field, the efficiency and the output power of the three-body system are slightly lower than the common TPV system.

With Γ fixed at $2\times10^{13}\,\mathrm{rad/s}$, we studied the change of Drude model plate's performance with ω_{p} and thickness t at $d=10\,\mathrm{nm}$ in **Fig. 9**. At $d=10\,\mathrm{nm}$, the three-body system's performance is superior in the area $1\times10^{15}\,\mathrm{rad/s}<\omega_{\mathrm{p}}<2\times10^{15}\,\mathrm{rad/s}$. This is to ensure that ω_{spp} is slightly larger than ω_{g}. Both $\eta_{\mathrm{F}}/\eta_{\mathrm{c}}$ and $P_{\mathrm{elF}}/P_{\mathrm{elc}}$ can obtain large values in the area of $10\,\mathrm{nm}<t<100\,\mathrm{nm}$. The maximum output power can reach $6.08\times10^{5}\ \mathrm{W/m^2}$. However, in the region close to $t=1\,\mu\mathrm{m}$, the efficiency can achieve greater value 43.9%. At this time, the output power has decreased but it is still more than twice the power of ordinary thermal photovoltaic systems.

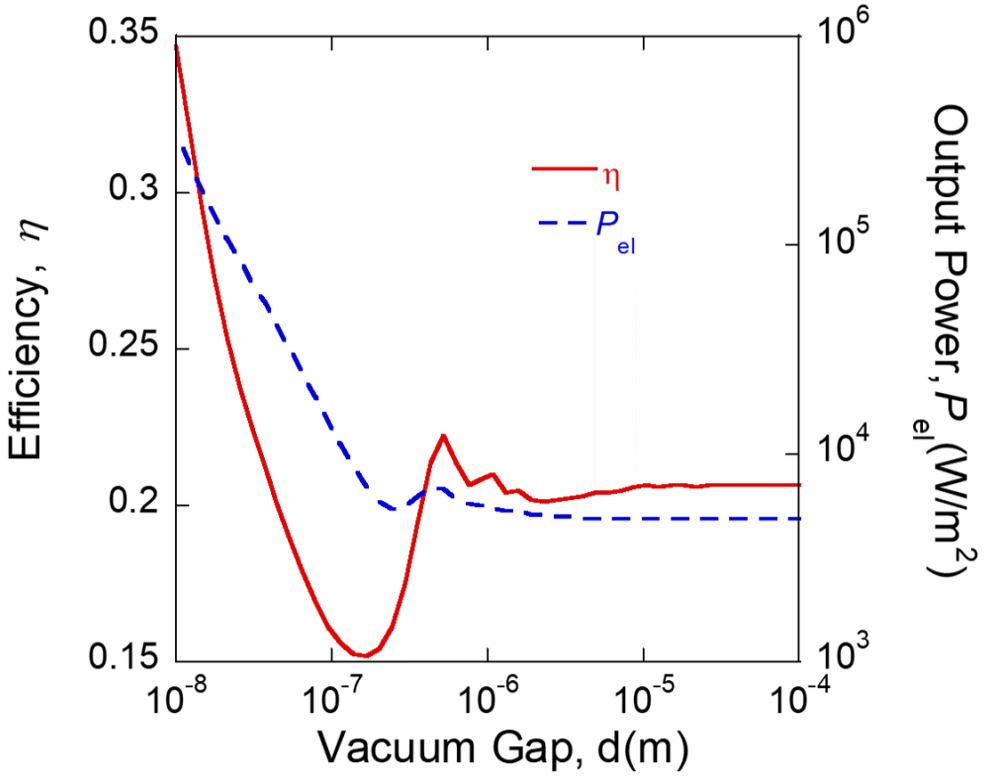

Fig. 8. The conversion efficiency (the red curve) and (b). the output power (the blue dashed line) are the variation of the performance of the optimized plate at $\omega_{\mathrm{p}} = 1.2\times10^{15}\ \mathrm{rad/s}, \Gamma = 2\times10^{13}\ \mathrm{rad/s}$ with the vacuum gap.

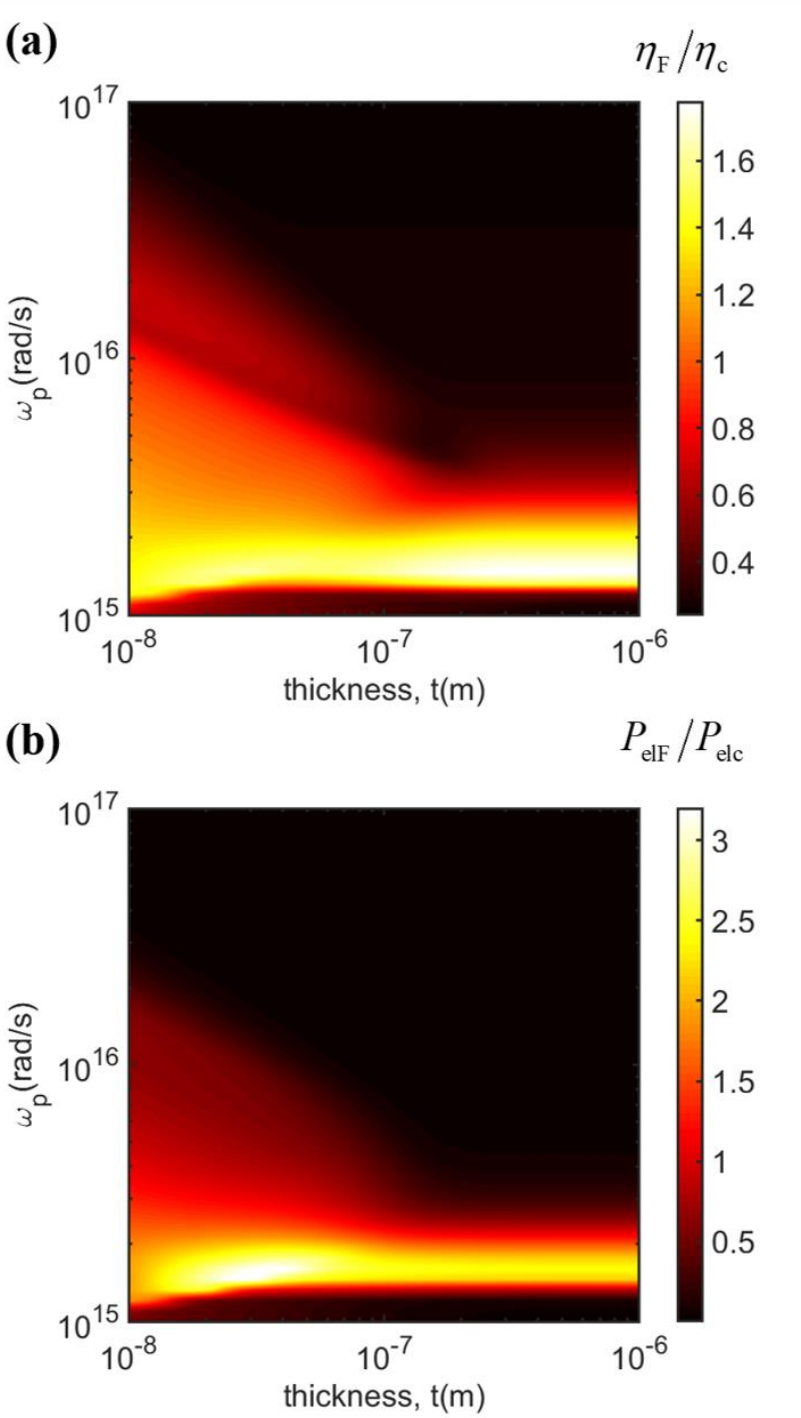

Fig. 9(a) conversion efficiency ratio η_F/η_c at $d=10$ nm (b) output power ratio P_{elF}/P_{elc} at $d=10$ nm. η_c and P_{elc} are the conversion efficiency and output power of the common TPV system respectively. η_F and P_{elF} are the conversion efficiency and output power of the three-body system respectively. The Γ of the Drude model plate is fixed at 2×10^{13} rad/s, while its ω_p and thickness t vary.

4. Conclusion

This paper studies the change in the performance of one-dimensional photonic crystals from the far-field to the near field and explains the mechanism that causes this change. Since one-dimensional photonic crystals are not suitable for near-field TPV systems, we optimized the Drude model plate as the spectrum control element for near-field TPV systems. Compared to Γ, ω_p and thickness t have a greater impact on the performance of the Drude model plate. But at this time, the middle plate can no longer filter, but works as a spectrum control element. By choosing parameters reasonably, the system can transfer energy through surface modes. And we can control the value of ω_{spp} to be slightly larger than ω_g, so that the power and efficiency of the system are greatly improved. The intermediate can provide a new heat exchange channel for the system. However, since the surface mode only exists in the near field, this spectral control element is not suitable for the far-field. Based on the calculation method of the radiant heat transfer of the multilayer structure, we can calculate the temperature of the intermediate components through thermodynamic equilibrium. In this way, we can further design more complex TPV systems in the near field and evaluate their efficiency and power.

References

[1] B. Zhao, K. Chen, S. Buddhiraju, G. Bhatt, M. Lipson, S. Fan, High-performance near-field thermophotovoltaics for waste heat recovery, Nano Energy, 41 (2017) 344-350.

[2] T. Bright, L. Wang, Z. Zhang, Performance of near-field thermophotovoltaic cells enhanced with a backside reflector, Journal of Heat Transfer, 136(6) (2014).

[3] R. Ovik, B. Long, M. Barma, M. Riaz, M. Sabri, S. Said, R. Saidur, A review on nanostructures of high-temperature thermoelectric materials for waste heat recovery, Renewable and sustainable energy reviews, 64 (2016) 635-659.

[4] A. Fiorino, L. Zhu, D. Thompson, R. Mittapally, P. Reddy, E. Meyhofer, Nanogap near-field thermophotovoltaics, Nature nanotechnology, 13(9) (2018) 806-811.

[5] J.I. Watjen, X. Liu, B. Zhao, Z. Zhang, A computational simulation of using tungsten gratings in near-field thermophotovoltaic devices, Journal of Heat Transfer, 139(5) (2017).

[6] A. Karalis, J. Joannopoulos, 'Squeezing'near-field thermal emission for ultra-efficient high-power thermophotovoltaic conversion, Scientific reports, 6 (2016) 28472.

[7] E. Tervo, E. Bagherisereshki, Z. Zhang, Near-field radiative thermoelectric energy converters: a review, Frontiers in Energy, 12(1) (2018) 5-21.

[8] F.K. Mbakop, N. Djongyang, D. Raïdandi, One–dimensional TiO 2/SiO 2 photonic crystal filter for thermophotovoltaic applications, Journal of the European Optical Society-Rapid Publications, 12(1) (2016) 23.

[9] F. O'Sullivan, I. Celanovic, N. Jovanovic, J. Kassakian, S. Akiyama, K. Wada, Optical characteristics of one-dimensional Si ⁄ Si O 2 photonic crystals for thermophotovoltaic applications, Journal of Applied Physics, 97(3) (2005) 033529.

[10] I. Celanovic, F. O'Sullivan, M. Ilak, J. Kassakian, D. Perreault, Design and optimization of one-dimensional photonic crystals for thermophotovoltaic applications, Optics letters, 29(8) (2004) 863-865.

[11] G. Liu, Y. Xuan, Y. Han, Q. Li, Investigation of one-dimensional Si/SiO 2 hotonic crystals for thermophotovoltaic filter, Science in China Series E: Technological Sciences, 51(11) (2008) 2031-2039.

[12] R.E. Nelson, A brief history of thermophotovoltaic development, Semiconductor Science and Technology, 18(5) (2003) S141.

[13] T.D. Rahmlow Jr, D.M. DePoy, P.M. Fourspring, H. Ehsani, J.E. Lazo-Wasem, E.J. Gratrix, Development of front surface, spectral control filters with greater temperature stability for thermophotovoltaic energy conversion, in: AIP Conference Proceedings, American Institute of Physics, 2007, pp. 59-67.

[14] D.N. Woolf, E.A. Kadlec, D. Bethke, A.D. Grine, J.J. Nogan, J.G. Cederberg, D.B. Burckel, T.S. Luk, E.A. Shaner, J.M. Hensley, High-efficiency thermophotovoltaic energy conversion enabled by a metamaterial selective emitter, Optica, 5(2) (2018) 213-218.

[15] P. Baldasaro, J. Raynolds, G. Charache, D. DePoy, C. Ballinger, T. Donovan, J. Borrego, Thermodynamic analysis of thermophotovoltaic efficiency and power density tradeoffs, Journal of Applied Physics, 89(6) (2001) 3319-3327.
[16] C. Fu, Z. Zhang, Nanoscale radiation heat transfer for silicon at different doping levels, International Journal of Heat and Mass Transfer, 49(9-10) (2006) 1703-1718.
[17] K. Park, W.P. King, Performance analysis of near-field thermophotovoltaic devices considering absorption distribution, in: ICHMT DIGITAL LIBRARY ONLINE, Begel House Inc., 2007.
[18] D. Polder, M. Van Hove, Theory of radiative heat transfer between closely spaced bodies, Physical Review B, 4(10) (1971) 3303.
[19] X. Liu, L. Wang, Z.M. Zhang, Near-field thermal radiation: recent progress and outlook, Nanoscale and microscale thermophysical engineering, 19(2) (2015) 98-126.
[20] R. St-Gelais, L. Zhu, S. Fan, M. Lipson, Near-field radiative heat transfer between parallel structures in the deep subwavelength regime, Nature nanotechnology, 11(6) (2016) 515.
[21] M.D. Whale, A fluctuational electrodynamic analysis of microscale radiative transfer and the design of microscale thermophotovoltaic devices, Massachusetts Institute of Technology, 1997.
[22] M. Whale, E.G. Cravalho, Modeling and performance of microscale thermophotovoltaic energy conversion devices, IEEE Transactions on Energy Conversion, 17(1) (2002) 130-142.
[23] A. Narayanaswamy, G. Chen, Surface modes for near field thermophotovoltaics, Applied Physics Letters, 82(20) (2003) 3544-3546.
[24] O. Ilic, M. Jablan, J.D. Joannopoulos, I. Celanovic, M. Soljačić, Overcoming the black body limit in plasmonic and graphene near-field thermophotovoltaic systems, Optics express, 20(103) (2012) A366-A384.
[25] R. Messina, P. Ben-Abdallah, Graphene-based photovoltaic cells for near-field thermal energy conversion, Scientific reports, 3(1) (2013) 1-5.
[26] J.L. Pan, H.K. Choy, C. Fonstad, Very large radiative transfer over small distances from a black body for thermophotovoltaic applications, IEEE Transactions on Electron Devices, 47(1) (2000) 241-249.
[27] M. Laroche, R. Carminati, J.-J. Greffet, Near-field thermophotovoltaic energy conversion, Journal of Applied Physics, 100(6) (2006) 063704.
[28] M. Francoeur, R. Vaillon, M.P. Mengüç, Thermal impacts on the performance of nanoscale-gap thermophotovoltaic power generators, IEEE Transactions on Energy Conversion, 26(2) (2011) 686-698.
[29] N. Vongsoasup, M. Francoeur, K. Hanamura, Performance analysis of near-field thermophotovoltaic system with 2D grating tungsten radiator, International Journal of Heat and Mass Transfer, 115 (2017) 326-332.
[30] M. Lim, S. Jin, S.S. Lee, B.J. Lee, Graphene-assisted Si-InSb thermophotovoltaic system for low temperature applications, Optics express, 23(7) (2015) A240-A253.
[31] M. Lim, S.S. Lee, B.J. Lee, Effects of multilayered graphene on the performance of near-field thermophotovoltaic system at longer vacuum gap distances, Journal of Quantitative Spectroscopy and Radiative Transfer, 197 (2017) 84-94.

[32] Y. Guo, Z. Jacob, Thermal hyperbolic metamaterials, Optics express, 21(12) (2013) 15014-15019.
[33] R.S. DiMatteo, P. Greiff, S.L. Finberg, K.A. Young-Waithe, H. Choy, M.M. Masaki, C.G. Fonstad, Enhanced photogeneration of carriers in a semiconductor via coupling across a nonisothermal nanoscale vacuum gap, Applied Physics Letters, 79(12) (2001) 1894-1896.
[34] R. DiMatteo, P. Greiff, D. Seltzer, D. Meulenberg, E. Brown, E. Carlen, K. Kaiser, S. Finberg, H. Nguyen, J. Azarkevich, M icron‐gap T hermo P hoto V oltaics (MTPV), in: AIP Conference Proceedings, American Institute of Physics, 2004, pp. 42-51.
[35] K. Hanamura, K. Mori, Nano‐gap tpv generation of electricity through evanescent wave in near‐field above emitter surface, in: AIP Conference Proceedings, American Institute of Physics, 2007, pp. 291-296.
[36] J.K. Tong, W.-C. Hsu, Y. Huang, S.V. Boriskina, G. Chen, Thin-film ‘thermal well’emitters and absorbers for high-efficiency thermophotovoltaics, Scientific reports, 5 (2015) 10661.
[37] S. Jin, M. Lim, S.S. Lee, B.J. Lee, Hyperbolic metamaterial-based near-field thermophotovoltaic system for hundreds of nanometer vacuum gap, Optics express, 24(6) (2016) A635-A649.
[38] R. Messina, M. Antezza, P. Ben-Abdallah, Three-body amplification of photon heat tunneling, Physical review letters, 109(24) (2012) 244302.
[39] M.-J. He, H. Qi, Y. Li, Y.-T. Ren, W.-H. Cai, L.-M. Ruan, Graphene-mediated near field thermostat based on three-body photon tunneling, International Journal of Heat and Mass Transfer, 137 (2019) 12-19.
[40] P. Ben-Abdallah, S.-A. Biehs, Near-field thermal transistor, Physical review letters, 112(4) (2014) 044301.
[41] L. Wang, Z. Zhang, Thermal rectification enabled by near-field radiative heat transfer between intrinsic silicon and a dissimilar material, Nanoscale and microscale thermophysical engineering, 17(4) (2013) 337-348.
[42] Z. Zheng, Y. Xuan, Enhancement or suppression of the near-field radiative heat transfer between two materials, Nanoscale and Microscale Thermophysical Engineering, 15(4) (2011) 237-251.
[43] Y.H. Kan, C.Y. Zhao, Z.M. Zhang, Near-field radiative heat transfer in three-body systems with periodic structures, Physical Review B, 99(3) (2019) 035433.
[44] K. Joulain, Y. Ezzahri, J. Drevillon, P. Ben-Abdallah, Modulation and amplification of radiative far field heat transfer: Towards a simple radiative thermal transistor, Applied Physics Letters, 106(13) (2015) 133505.
[45] I. Latella, A. Pérez-Madrid, J.M. Rubi, S.-A. Biehs, P. Ben-Abdallah, Heat engine driven by photon tunneling in many-body systems, Physical Review Applied, 4(1) (2015) 011001.

[46] H. Prod'homme, J. Ordonez-Miranda, Y. Ezzahri, J. Drévillon, K. Joulain, VO2-based radiative thermal transistor with a semi-transparent base, Journal of Quantitative Spectroscopy and Radiative Transfer, 210 (2018) 52-61.
[47] W. Gu, G.-H. Tang, W.-Q. Tao, Thermal switch and thermal rectification enabled by near-field radiative heat transfer between three slabs, International Journal of Heat and Mass Transfer, 82 (2015) 429-434.
[48] X. Liu, Z.M. Zhang, High-performance electroluminescent refrigeration enabled by photon tunneling, Nano Energy, 26 (2016) 353-359.
[49] E.D. Palik, Handbook of optical constants of solids, Academic press, 1998.
[50] J.A. González-Cuevas, T.F. Refaat, M.N. Abedin, H.E. Elsayed-Ali, Modeling of the temperature-dependent spectral response of in 1–χ ga χ sb infrared photodetectors, Optical Engineering, 45(4) (2006) 044001.
[51] D. Feng, E.J. Tervo, S.K. Yee, Z.M. Zhang, Effect of Evanescent Waves on the Dark Current of Thermophotovoltaic Cells, Nanoscale and Microscale Thermophysical Engineering, 24(1) (2020) 1-19.
[52] N. Ashcroft, N. Mermin, Solid State Physics Saunders College Publishing, in, Philadelphia, 1976.
[53] J.-Y. Chang, Y. Yang, L. Wang, Tungsten nanowire based hyperbolic metamaterial emitters for near-field thermophotovoltaic applications, International Journal of Heat and Mass Transfer, 87 (2015) 237-247.
[54] Z.M. Zhang, Nano/microscale heat transfer, 2007.
[55] S. Rytov, Y.A. Kravtsov, V. Tatarskii, Principles of statistical radiophysics. Vol. 4, wave propagation, in, Berlin: Springer, 1989.
[56] J.E. Sipe, New Green-function formalism for surface optics, JOSA B, 4(4) (1987) 481-489.
[57] M. Francoeur, M.P. Mengüç, R. Vaillon, Solution of near-field thermal radiation in one-dimensional layered media using dyadic Green's functions and the scattering matrix method, Journal of Quantitative Spectroscopy and Radiative Transfer, 110(18) (2009) 2002-2018.
[58] A. Narayanaswamy, G. Chen, Thermal emission control with one-dimensional metallodielectric photonic crystals, Physical Review B, 70(12) (2004) 125101.
[59] A. Narayanaswamy, G. Chen, Thermal radiation in 1D photonic crystals, Journal of Quantitative Spectroscopy and Radiative Transfer, 93(1-3) (2005) 175-183.
[60] B.J. Lee, Z.M. Zhang, Lateral Shifts in Near-Field Thermal Radiation with Surface Phonon Polaritons, Nanoscale and Microscale Thermophysical Engineering, 12(3) (2008) 238-250.
[61] E.N. Economou, Surface Plasmons in Thin Films, Physical Review, 182(2) (1969) 539-554.